



RESEARCH ARTICLE

10.1002/2014RS005584

Key Points:

- A fast and accurate STD forward operator is developed
- The tangent linear and adjoint code is constructed
- The operators are tailored for data assimilation and travel time tomography

Correspondence to:

F. Zus,
zusflo@gfz-potsdam.de

Citation:

Zus, F., G. Dick, S. Heise, and J. Wickert (2015), A forward operator and its adjoint for GPS slant total delays, *Radio Sci.*, 50, doi:10.1002/2014RS005584.

Received 22 AUG 2014

Accepted 8 APR 2015

Accepted article online 15 APR 2015

A forward operator and its adjoint for GPS slant total delays

Florian Zus¹, Galina Dick¹, Stefan Heise¹, and Jens Wickert¹

¹Helmholtz Centre Potsdam, GFZ German Research Centre for Geosciences, Potsdam, Germany

Abstract In a recent study we developed a fast and accurate algorithm to compute Global Positioning System (GPS) Slant Total Delay (STDs) utilizing numerical weather model data. Having developed a forward operator we construct in this study the tangent linear (adjoint) operator by application of the chain rule of differential calculus in forward (reverse) mode. Armed with these operators we show in a simulation study the potential benefit of GPS STDs in inverse modeling. We conclude that the developed operators are tailored for three (four)-dimensional variational data assimilation and/or travel time tomography.

1. Introduction

Radio signals which are transmitted by Global Positioning System (GPS) satellites and received by a ground-based station allow the estimation of the Zenith Total Delay (ZTD). The ZTD, which is closely related to the Integrated Water Vapor above the station, is the basic observable in GPS meteorology [Bevis et al., 1992]. ZTD data are available from several station networks in Europe in Near Real Time (NRT) such as from the European Meteorological Network Global Navigation Satellite Systems (GNSS) Water Vapor Program and assimilation studies have shown that the usage of ZTD data improve the forecast skill [see, e.g., Vedel and Huang, 2004]. Consequently, ZTD data are assimilated operationally at several weather agencies in Europe [Poli et al., 2007; Bennitt and Jupp, 2012]. Clearly, the ZTD is of limited value because it does not contain information about horizontal (vertical) atmospheric gradients. The Slant Total Delays (STDs), i.e., the atmospheric induced signal travel time delays between the station and the satellites in view, can provide additional information about local atmospheric gradients. The German Research Center for Geosciences (GFZ) estimates STD data for a station network in Germany in NRT [Deng et al., 2011], but conclusive assimilation studies are not possible without a rapid and accurate forward operator.

An algorithm to compute the STD for a station-satellite link given the refractivity field of a Numerical Weather Model (NWM), in other words a forward operator, was recently suggested [Zus et al., 2012]. The unique feature of this algorithm is that the posed two-point Boundary Value Problem (BVP) is solved by a finite difference scheme where the positions of the satellite and the station are automatically part of the solution. In a follow-on study the algorithm was modified such that STDs are computed with an unprecedented speed and precision [Zus et al., 2014a]. This modified algorithm is certainly useful for forward modeling in geodesy [Zus et al., 2014b], but for inverse modeling in meteorology two ingredients are missing; the tangent linear operator and its adjoint. The derivation of the tangent linear and adjoint operator is subject of this study. We test their functionality in inverse modeling and show the potential benefit of a set of STDs over the ZTD for a single station. We would like to stress that this study differs from a comparable study by Eresmaa et al. [2008] in several respects. At first, our forward operator takes into account the so-called geometric delay and is thus based on the definition of the STD and not an approximation of it. Second, our forward operator solves the posed two-point BVP in a rigorous way. Third, we validate our forward operator with state-of-the-art ray trace software packages [Nafisi et al., 2012] in order to provide at least a rough estimate for the accuracy of the forward operator.

After this introduction we describe in section 2 the construction of the forward, tangent linear, and adjoint operator. In section 3 we show the functionality of the operators. In section 4 we compare GPS- and NWM-based STDs. The conclusion is given in section 5.

2. The Forward and Adjoint Operator

2.1. The Slant Total Delay

The STD is postulated as confined to a plane defined by the location of the station, Earth's center (center of an osculating sphere), and the location of the satellite [Zus et al., 2014a]; this is equivalent to neglecting

out-of-plane bending. It is convenient to rotate the local frame of reference at the station such that the x axis points to the satellite. In this local frame of reference the STD reads as [Hofmann-Wellenhof et al., 1992]

$$S = \int_a^b n(x, y(x)) \cdot \sqrt{1 + y'(x)^2} dx + a - b \quad (1)$$

where a and b denote the x coordinate of the station and the satellite, respectively, and n denotes the index of refraction. The ray trajectory equation is derived from calculus of variation and reads as

$$y''(x) - \left[\frac{n_y(x, y)}{n(x, y)} - \frac{n_x(x, y)}{n(x, y)} y'(x) \right] \cdot [1 + y'(x)^2] = 0 \quad (2)$$

where the subscripts x and y denote partial derivatives. With the position of the station and the satellite

$$\begin{aligned} y(a) &= 0 \text{ and} \\ y(b) &= 0 \end{aligned} \quad (3)$$

the ray trajectory equation is a two-point BVP.

The ray trajectory equation is simplified by two approximations valid under typical atmospheric conditions [Zus et al., 2014a]. At first, we note that the index of refraction is close to unity and therefore

$$\frac{1}{n(x, y)} \sim 1 \quad (4)$$

Second, the partial derivatives of the refractive index is approximated by

$$\begin{aligned} n_x(x, y) &\sim n_h(x, y) \cdot h_x(x, y) \text{ and} \\ n_y(x, y) &\sim n_h(x, y) \cdot h_y(x, y) \end{aligned} \quad (5)$$

where h denotes the height above the osculating sphere. In essence, we neglect horizontal gradients in the determination of the ray trajectory. The bent raypath is due to the refractive index lapse rate n_h .

The relation between the index of refraction and the atmospheric state is given through $n = 10^{-6}N + 1$, where the refractivity N is a function of the pressure, the temperature, and the specific humidity [Thayer, 1974]. Provided that the refractivity is known, the ray trajectory and subsequently the STD can be computed. Since a NWM provides refractivity at specific grid points, the refractivity at an arbitrary point must be determined by an interpolation algorithm. Below (above) the lowest (highest) NWM layer the refractivity is obtained by extrapolation. The gradient of the refractivity at an arbitrary point is obtained by differentiation of the interpolation algorithm.

2.2. The Forward Operator

The forward operator follows the STD algorithm proposed by Zus et al. [2014a]. This algorithm is a two-step procedure; in the first step the ray trajectory is determined and in the second step the numerical quadrature is performed.

Step 1. The ray trajectory equation is solved by a finite difference scheme. The basic idea is to define a node sequence $X = [x_1, \dots, x_n]$ and to insert for this node sequence the derivatives of y with respect to x by finite differences (derivatives of low-order Lagrange interpolating polynomials). Therefore, the ray trajectory equation turns into a nonlinear system of equations

$$F(Y) = 0 \quad (6)$$

where $Y = [y_1, \dots, y_n]$ denotes the solution vector. The nonlinear system of equations is solved by Newton's method. Let Y_r denote the solution vector at the iteration step r . The solution vector Y_{r+1} at the iteration step $r + 1$ is obtained by solving the system of linear equations

$$\mathbf{J}[Y_r] \cdot (Y_{r+1} - Y_r) = -F(Y_r) \quad (7)$$

where the Jacobian \mathbf{J} is determined analytically. In each Newton-Raphson iteration the linear system of equations is solved by a lower upper decomposition. The first guess vector Y_0 corresponds to the straight line between the satellite and the station; that is, $Y_0 = [0, \dots, 0]$. A remarkable feature is that for elevation angles $\geq 3^\circ$ a single Newton-Raphson iteration is sufficient to compute STDs with a precision of 1 mm. In this case the solution vector is given through

$$Y = -\mathbf{J}^{-1}[Y_0] \cdot F(Y_0) \tag{8}$$

Step 2. Once the ray trajectory is determined the composite Simpson rule is applied in the numerical quadrature.

The forward operator H is now defined as follows; given a station-satellite link and the refractivity field \mathbf{x} determine the STD, that is

$$S = H[\mathbf{x}] \tag{9}$$

Note that the refractivity field \mathbf{x} represents a vector which stores the entire NWM refractivity field. In a numerical weather prediction (NWP) context the forward operator is expressed directly in terms of the pressure, temperature, and specific humidity. This additional difficulty of the (full) forward operator that is required in a NWP context is not considered in this study.

2.3. The Tangent Linear and Adjoint Operator

The tangent linear operator \mathbf{H} is defined as

$$\mathbf{H} = \frac{\partial H}{\partial \mathbf{x}} \tag{10}$$

and the adjoint operator \mathbf{H}^* is defined as

$$\mathbf{H}^* = \mathbf{H}^T \tag{11}$$

In essence, the tangent linear (adjoint) operator is obtained by differentiation of the STD algorithm.

2.3.1. The Rigorous Step-By-Step Derivation

To allow for an exact and step-by-step derivation, it is convenient to view the forward operator as a composite of two operators: the determination of the ray trajectory H_1 and the numerical quadrature H_2 . Hence, H is viewed as a composite of two operators H_1 and H_2 , that is

$$H[\mathbf{x}] = H_2[H_1[\mathbf{x}]] \tag{12}$$

The tangent linear operator is obtained by application of the chain rule of differential calculus

$$\mathbf{H} = \left(\frac{\partial H_2}{\partial H_1} \right) \left(\frac{\partial H_1}{\partial \mathbf{x}} \right) \tag{13}$$

and the adjoint operator is obtained by the transpose of the tangent linear operator

$$\mathbf{H}^* = \left(\frac{\partial H_1}{\partial \mathbf{x}} \right)^T \left(\frac{\partial H_2}{\partial H_1} \right)^T \tag{14}$$

In tangent linear and adjoint model development the above matrices are not explicitly determined. In fact, one is only concerned with obtaining the result of a matrix/vector product $\mathbf{H} \delta \mathbf{x}$ or $\mathbf{H}^* \delta \mathbf{v}$ where $\delta \mathbf{x}$ and $\delta \mathbf{v}$ denote vectors. The matrix/vector products are referred to as the tangent linear model (TLM) and adjoint (ADJ) code, respectively. The forward operator H is referred to as the nonlinear Model (NLM). The TLM (ADJ) code is constructed by rigorous application of the chain rule of differential calculus in forward (reverse) mode [Giering and Kaminski, 1998].

2.3.2. The Fast Differentiation

We recall that the STD is the signal travel time delay (measured as a distance) between the station and the satellite. The ray trajectory follows from calculus of variation, and thus, for a refractivity field perturbation the first-order travel time perturbation δS is given through

$$\delta S = \int_a^b \delta n(x, y(x)) \cdot \sqrt{1 + y'(x)^2} dx \tag{15}$$

where δn denotes the refractive index perturbation along the (initial) ray trajectory. In other words, there is no need to differentiate the ray trajectory. It is sufficient to differentiate the refractive index along the ray trajectory. Recognizing this, in this study, we use the fast differentiation.

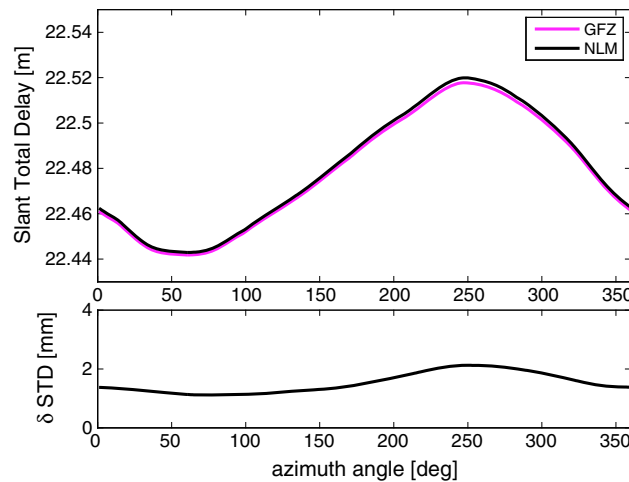


Figure 1. (top) Slant Total Delays (m) at an elevation angle of 5° as a function of the azimuth angle for Wettzell (1 January 2008, 0 UTC). Different colors correspond to different solutions; GFZ and NLM. (bottom) The difference of Slant Total Delays (mm) as a function of the azimuth angle (NLM minus GFZ).

based on a FORTRAN implementation, the Intel FORTRAN compiler, and an ordinary PC (Core2Quad Intel processor, 2.5 GHz, 2 GB RAM) using a single core. Note that our comparisons allow us to estimate the precision but not the accuracy because common errors of the STDs and the reference STDs, e.g., due the same interpolation approach for the refractivity, cancel.

For this reason we made use of data from a ray trace comparison campaign [Nafisi et al., 2012]. The participants of the campaign were provided with the Integrated Forecast System (IFS) analysis of the European Centre for Medium-Range Weather Forecasts (ECMWF) for a station in Japan (Tsukuba) and for a station in Germany (Wettzell) and computed ray-traced tropospheric delays for an elevation angle of 5° (every degree in azimuth). Strictly speaking, the tropospheric delays are not STDs since the tropospheric delays are not determined for the GPS but very long baseline interferometry (VLBI) [Zus et al., 2014b]. However, for an elevation angle of 5° the differences between GPS and VLBI tropospheric delays are negligible (about 1 mm). From the ray trace comparison campaign we estimate the accuracy of the STD algorithm to be on the 1 mm level close to the

zenith and on the 1 cm level for an elevation angle of 5° [Zus et al., 2014a].

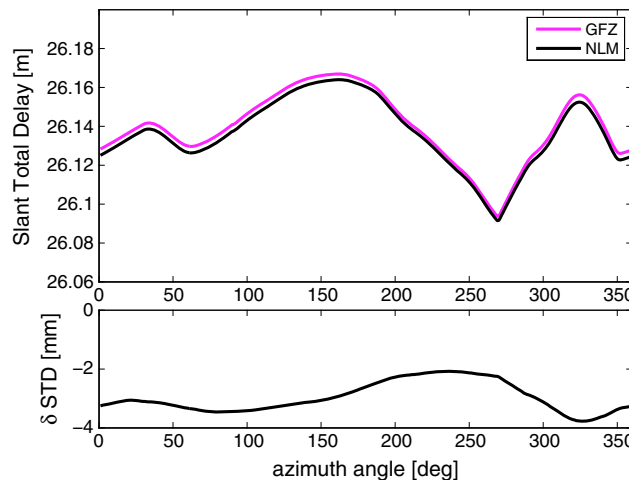


Figure 2. (top) Slant Total Delays (m) at an elevation angle of 5° as a function of the azimuth angle for Tsukuba (8 August 2008, 0 UTC). Different colors correspond to different solutions; GFZ and NLM. (bottom) The difference of Slant Total Delays (mm) as a function of the azimuth angle (NLM minus GFZ).

2.4. Test for Correctness and Efficiency

Since the NLM follows closely the STD algorithm proposed by Zus et al. [2014a], it shares the same properties. Numerous tests were conducted to estimate the speed and precision of this algorithm. We compared with reference STDs which were obtained by the same algorithm but a refined node sequence. We also compared with reference STDs which were obtained by a classic ray tracing algorithm (the ray trajectory equation is transformed to a system of two first-order differential equations and solved by a fourth-order Runge-Kutta routine). In summary, extensive tests indicate that our algorithm predicts STDs with a precision of about 1 mm for any elevation angle $\geq 1^\circ$ and irrespectively of the elevation angle about 2000 STDs per second are computed. This data throughput is

Here we make a similar test to validate the NLM. We also conduct this test to reveal and explain a discrepancy between the NLM and our previously proposed STD algorithm, hereinafter denoted as GFZ. Figures 1 and 2 show the STDs (NLM and GFZ) as a function of the azimuth angle for Tsukuba and Wettzell, respectively. The differences of the STDs (NLM minus GFZ) shown in Figures 1 (bottom) and 2 (bottom) are not due to the differences between GPS and VLBI tropospheric delays (the NLM computes GPS tropospheric delays, while the GFZ computes VLBI tropospheric delays in this example). The differences are due to a different interpolation algorithm for the refractivity.

The GFZ solution is based on the following approach: the temperature (and specific humidity) is interpolated linearly, the pressure is interpolated logarithmically, and then the refractivity is computed. The NLM solution is based on the following approach: the refractivity is computed from the temperature, the specific humidity, and the pressure at each grid node and then the refractivity is interpolated logarithmically. However, since the differences in Figures 1 and 2 are well below 1 cm we conclude that the accuracy of the NLM is comparable to the accuracy of the GFZ. Finally, we note another difference between the NLM and the GFZ, which, however, is only relevant for the data throughput; the NLM utilizes an elevation angle-dependent number of Newton-Raphson iterations while the GFZ utilizes by default two Newton-Raphson iterations. In particular, a single Newton-Raphson iteration for any elevation angle $\geq 3^\circ$ increases the data throughput to about 3000 STDs per second.

The TLM and ADJ codes are tested for correctness using the standard comparison of the TLM and finite difference-derived NLM gradients to check correctness of the TLM

$$\lim_{\delta \mathbf{x} \rightarrow 0} \frac{H[\mathbf{x} + \delta \mathbf{x}] - H[\mathbf{x}]}{\mathbf{H} \delta \mathbf{x}} = 1 \quad (16)$$

and the definition of the TLM and the ADJ

$$(\mathbf{H} \delta \mathbf{x}) \cdot \delta \mathbf{v} = \delta \mathbf{x} \cdot (\mathbf{H}^* \delta \mathbf{v}) \quad (17)$$

to check consistency of the ADJ. The data throughput for the ADJ code is about one third of the data throughput of the NLM code.

Armed with the NLM, TLM, and ADJ code we show how they perform in inverse modeling.

3. Minimizing a Cost Function

We consider the following inverse problem; given the observations \mathbf{y} and the background refractivity field \mathbf{x}_b , determine the most probable refractivity field \mathbf{x}_a . By taking into account Bayes's theorem under the assumption that background errors and observation errors have Gaussian statistics and are independent of each other, the most probable refractivity field is the one that minimizes the cost function [see, e.g., Daley, 1991]

$$C[\mathbf{x}] = \frac{1}{2} (\mathbf{x} - \mathbf{x}_b)^T \mathbf{B}^{-1} (\mathbf{x} - \mathbf{x}_b) + \frac{1}{2} (\mathbf{y} - H[\mathbf{x}])^T \mathbf{R}^{-1} (\mathbf{y} - H[\mathbf{x}]) \quad (18)$$

Here \mathbf{B} and \mathbf{R} denote the background and observation error covariance matrix, respectively. The diagonal elements of the matrix \mathbf{B} store the squared refractivity error variances and the off-diagonal elements store the refractivity error covariances. Likewise, the diagonal elements of the matrix \mathbf{R} store the squared observation error variances and the off-diagonal elements store the observation error covariances. The minimum of the cost function C must be determined iteratively since the forward operator H is a nonlinear function of the refractivity field \mathbf{x} . In order to demonstrate the functionality of the NLM, TLM, and ADJ, it is sufficient to consider a single iteration in the minimization. We choose the first guess refractivity field to be equal to the background refractivity field and obtain the most probable refractivity field through (refer to Appendix A).

$$\mathbf{x}_a = \mathbf{x}_b + \mathbf{B} \mathbf{H}^T [\mathbf{x}_b] (\mathbf{H} [\mathbf{x}_b] \mathbf{B} \mathbf{H}^T [\mathbf{x}_b] + \mathbf{R})^{-1} (\mathbf{y} - H[\mathbf{x}_b]) \quad (19)$$

We perform the following simulation; given a set of true STDs for a single station, add noise to mimic observed STDs and alter the background refractivity field such that the analysis STDs are closer to the true STDs than the background STDs. In particular, in the limit of error-free observations the analysis STDs must approach the observed (true) STDs, that is, $\mathbf{y} = H[\mathbf{x}_a]$.

In our simulation the background refractivity field is a Global Forecast System (GFS) analysis of the National Centers for Environmental Prediction valid for 26 June 2013, 12 UTC. The NWM data have a horizontal resolution of 1° by 1° and are available on 26 pressure levels. For a single station in Germany (Potsdam) we compute a set of background STDs. The spacing in azimuth is 30° . The elevation angles are $3^\circ, 5^\circ, 7^\circ, 10^\circ, 15^\circ, 20^\circ, 30^\circ, 50^\circ, 70^\circ$, and 90° . The true STDs are obtained by utilizing the background refractivity field but shifting the azimuth angles by 45° . The observed STDs are obtained from the true STDs by adding Gaussian noise

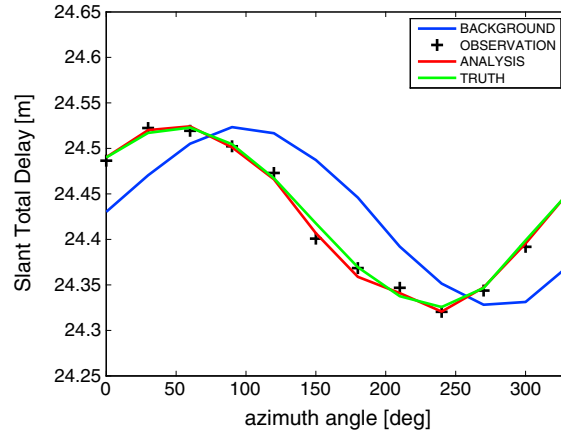


Figure 3. Slant Total Delays (m) at an elevation angle of 5° as a function of the azimuth angle for Potsdam (26 June 2013, 12 UTC). Different colors correspond to the background, the analysis, and the truth. The observations (black crosses) are obtained from the truth by adding Gaussian noise. The 1 sigma deviation is 0.03 %. The analysis is obtained by variational data analysis. For details, refer to the text.

with zero mean. The standard deviations are a fraction p of the observations \mathbf{y} . Hence, the observation error covariance matrix \mathbf{R} reads as

$$R_{ij} = p^2 y_i y_j \delta_{ij} \quad (20)$$

where δ_{ij} denotes Kronecker's delta. Note that in practice, the observations will have correlated errors [see, e.g., Järvinen et al., 2007]. Further we assume that the refractivity error variances are a fraction q of the refractivity field \mathbf{x} and that there are no horizontal but only vertical error correlations. In essence, the background error covariance matrix \mathbf{B} reads as

$$B_{ij} = q^2 x_i x_j \exp(-(|h_i - h_j|)^2 / \zeta^2) \delta(\phi_i - \phi_j) \delta(\varphi_i - \varphi_j) \quad (21)$$

where ϕ_i , φ_i , and h_i denote the longitude, latitude, and height of the i th grid point, respectively. The delta distribution δ removes horizontal correlations. In our simulation the fractional refractivity error variance is chosen

to be 1% and the vertical correlation length ζ is chosen to be 500 m. Note that we perform a simulation study and not an assimilation study (we are concerned with the functionality of the NLM, TLM, and ADJ) such that the choice of the background error covariance matrix is not crucial. The specific choice of 1% for the fractional refractivity error variance is rational insofar as it corresponds to the typical standard deviation between GPS Radio Occultation and NWM refractivity profiles [see, e.g., Zus et al., 2011].

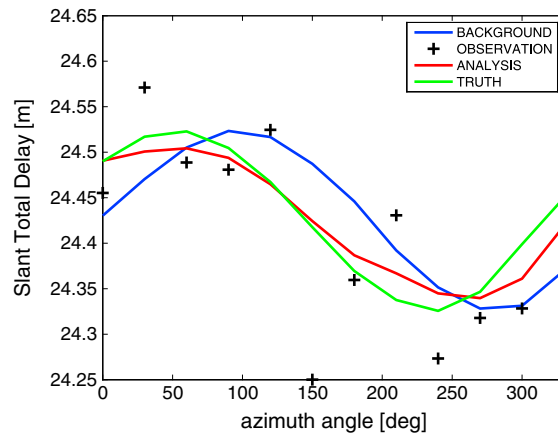


Figure 4. Slant Total Delays (m) at an elevation angle of 5° as a function of the azimuth angle for Potsdam (26 June 2013, 12 UTC). Different colors correspond to the background, the analysis, and the truth. The observations (black crosses) are obtained from the truth by adding Gaussian noise. The 1 sigma deviation is 0.3%. The analysis is obtained by variational data analysis. For details, refer to the text.

Figures 3 and 4 show the STDs (background, observation, analysis, and truth) as a function of the azimuth angle for the observation error of 0.03% and 0.3%, respectively (the elevation angle is 5°). From Figure 3 we conclude that in the limit of perfect observations, the analysis STDs equal the true STDs, and from Figure 4 we conclude that for imperfect observations, the analysis STDs approach the true STDs as well. Hence, the Figures 3 and 4 prove the functionality of the NLM, TLM, and ADJ.

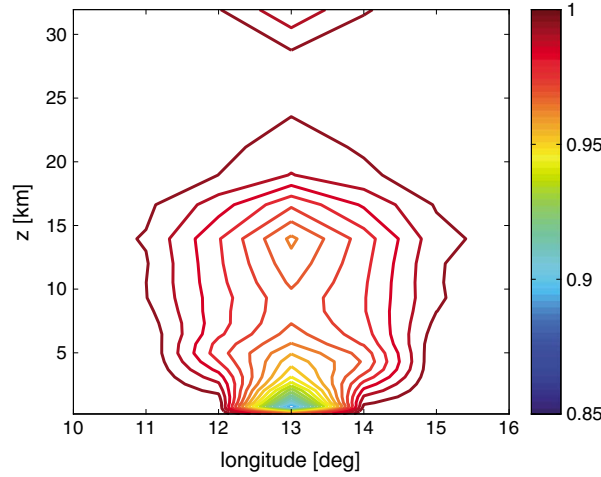


Figure 5. Contour plot showing the ratio of the a posteriori variance and background variance for a vertical cross section (latitude of 52°). The observation error is 0.3%. For details, refer to the text.

considered a rough measure for the asymmetry of the refractivity field (refer to Appendix B). Figures 6 and 7 show the tropospheric delay gradient vectors for the two observation errors, respectively. The impact is not restricted to the location of the station but spread over an area of about 5° by 5°. This can be explained by the observation geometry and the sensitivity of the STDs on the refractivity; due to the exponential decrease of the refractivity with height the sensitivity of STDs decreases with height and hence the distance (see Figure 5). Note that an error-free STD close to the zenith, i.e., an error-free ZTD, has no impact. It is also important to note that what we see in Figures 6 and 7 is the raw impact of a set of STDs. In practice, the nonvanishing flow field-dependent horizontal correlations of the background error covariance matrix will alter the impact area in a physical consistent way. Finally, Figure 8 shows the tropospheric delay gradient vectors for the observation error 0.3% and a more realistic observation geometry (azimuth angles are selected randomly and elevation angles are obtained through $\epsilon = 90 - 87\sqrt{r}$ where $r \in [0, 1]$ is obtained from a random number generator). Clearly, the impact is reduced but the twist in the tropospheric delay gradient vectors is preserved.

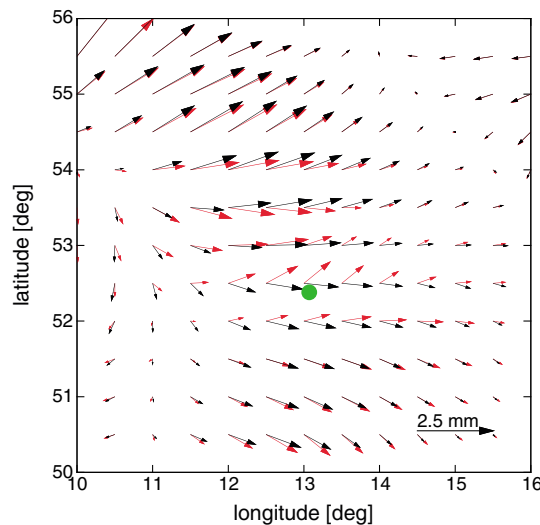


Figure 6. Map of tropospheric delay gradient vectors in the vicinity of Potsdam (26 June 2013, 12 UTC). The black (red) arrows correspond to the background (analysis) refractivity field. The green dot indicates the location of the station providing STDs with an observation error of 0.03 %. For details, refer to the text.

In order to show how the uncertainty in the refractivity field grows away from the single station, we approximate the a posteriori covariance matrix through

$$\mathbf{A} = (\mathbf{B}^{-1} + \mathbf{H}^T[\mathbf{x}_b]\mathbf{R}^{-1}\mathbf{H}[\mathbf{x}_b])^{-1} \quad (22)$$

In particular, for the observation error 0.3%, Figure 5 shows the ratios of the a posteriori variance and background variances, i.e., $r_i = \sqrt{A_{ii}/B_{ii}}$, for a vertical cross section (latitude 52°). Basically, these ratios are < 1 inside the cone defined by the lowest elevation STDs that are included in the analysis. Outside the cone the ratios are about 1 which means that the refractivity field is not affected by the STDs.

Next, we utilize tropospheric delay gradient maps to gain insight into the impact of a set of STDs in the vicinity of a single station. The tropospheric delay gradients can be considered

3.1. Vertical Profiling of Refractivity Using a Single Station

In the previous section we showed that the developed operators can be used to extract asymmetric information from STDs. In this section we show that the developed operators can be used to extract vertical gradient information from STDs as well.

Initially we assume that in the vicinity of any station, the refractivity field is spherically layered. Therefore, it is sufficient to consider a single refractivity profile, i.e., $N = N(h)$. Still, provided that the station is close to the ground and provided that the elevation angles are positive, the determination of the refractivity from STDs is an ill-posed problem [Lowry et al., 2002; Wu et al., 2014]. Recognizing this, we make use of the same algebra (regularization method) that is used in the previous section. Some modifications are convenient. For example, it is convenient to express the refractivity profile as follows

$$N(h) = N_0 \cdot \exp(-[h - (j-1) \cdot \Theta] \cdot \xi_j) \prod_{k=1}^{j-1} \exp(-\Theta \cdot \xi_k) \quad (23)$$

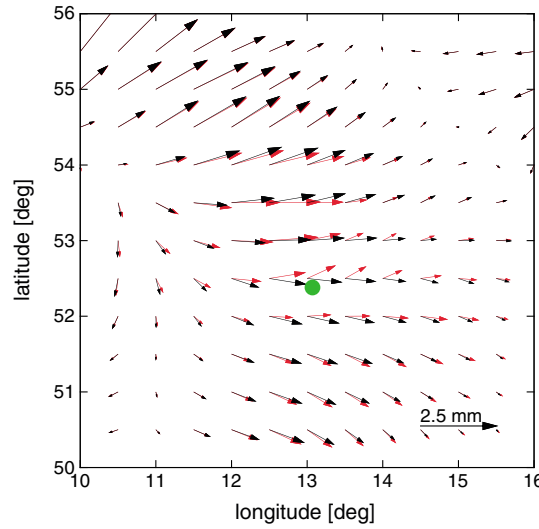


Figure 7. Same as in Figure 6, except that the observation error is 0.3% instead of 0.03%.

profile \mathbf{x}_0 . The inverse problem is solved by minimizing the corresponding cost function. We choose the first guess refractivity profile to be equal to the background refractivity profile and obtain the refractivity profile \mathbf{x}_{i+1} at the iteration step $i + 1$ through (refer to Appendix A)

$$\mathbf{x}_{i+1} = \mathbf{x}_i + \mathbf{P}[\mathbf{x}_i]^{-1} [\mathbf{H}^T[\mathbf{x}_i] \mathbf{R}^{-1} (\mathbf{y} - H[\mathbf{x}_i]) - \mathbf{B}^{-1} (\mathbf{x}_i - \mathbf{x}_b)] \quad (25)$$

where

$$\mathbf{P}[\mathbf{x}_i] = \mathbf{B}^{-1} + \mathbf{H}^T[\mathbf{x}_i] \mathbf{R}^{-1} \mathbf{H}[\mathbf{x}_i] \quad (26)$$

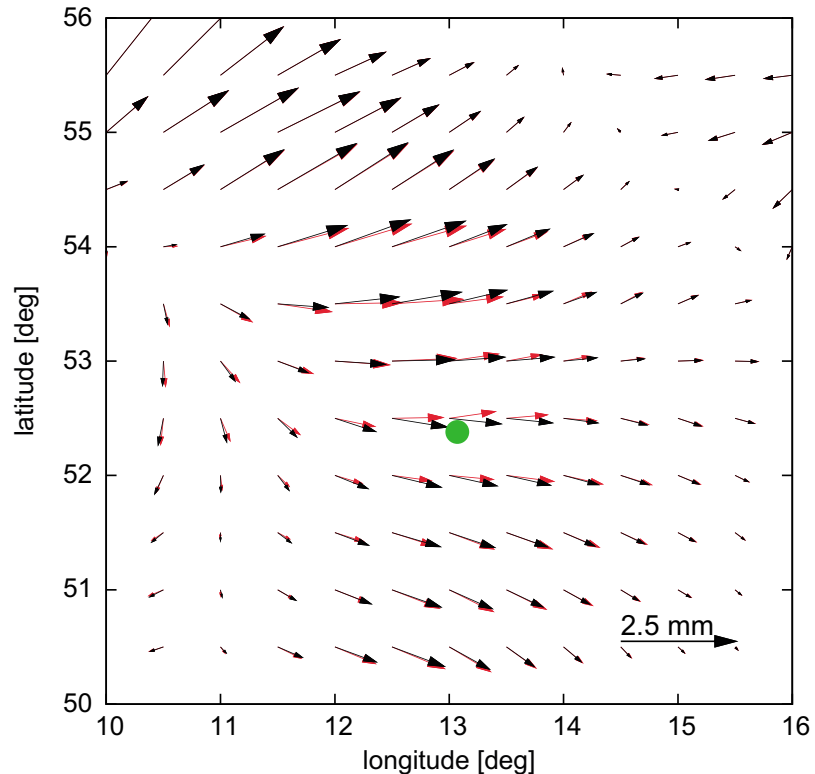


Figure 8. Same as in Figure 6, except that the observation error is 0.3% instead of 0.03% and the observation geometry corresponds to the GPS.

for $(j - 1) \cdot \Theta \leq h < j \cdot \Theta$, where Θ denotes the layer thickness, N_0 denotes the refractivity at zero height, and ξ_j for $j = 1, \dots, m$ denotes a set of inverse-scale heights. While in the previous section \mathbf{x} represents the refractivity field, in the following \mathbf{x} represents the single refractivity profile which is expressed in terms of the refractivity at zero height and the set of inverse-scale heights, i.e., $\mathbf{x} = [N_0, \xi_1, \dots, \xi_m]$. The corresponding forward operator reads as

$$H[\mathbf{x}] = S_R(N_0, \xi_1, \dots, \xi_m) \quad (24)$$

where S_R stands for the algorithm that computes STDs utilizing the single refractivity profile. The tangent linear (adjoint) operator is expressed in terms of the refractivity at zero height and the set of inverse-scale heights as well.

We consider the following inverse problem; given the observations \mathbf{y} and the background refractivity profile \mathbf{x}_b determine the most probable refractivity

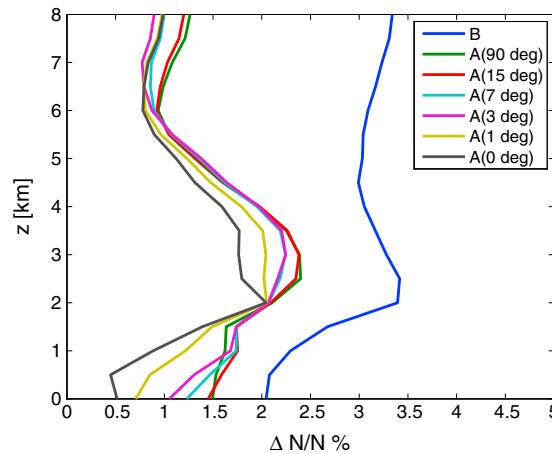


Figure 9. The fractional refractivity error of the analysis (A) as a function of the height. In total 361 refractivity profiles in the vicinity of Potsdam (26 June 2013, 12 UTC) enter the statistic. Different colors correspond to different sets of STDs that are used in the variational data analysis (elevation cut-off angles 0°, 1°, 3°, 7°, 15°, and 90°). In the latter case a single ZTD is used. The observation error is 0.03 %. The blue line corresponds to the fractional refractivity error of the background (B). For details, refer to the text.

sufficient to determine an error-free refractivity profile. However, if the refractivity at zero height is unknown and an increasing number of layers is considered, the inverse problem is increasingly ill conditioned. In essence, the condition number of the matrix \mathbf{P} (the ratio of the largest to the smallest singular value) is increasing with an increasing number of layers. We also note that the condition number of the matrix \mathbf{P} depends on the set of STDs; the lower the elevation cut-off angle, the smaller the condition number. This already indicates that there is a benefit of STDs on top of the ZTD. In order to mimic a reasonable refractivity profile, we choose the vertical resolution to be $\Theta = 500$ m and the number of layers to be $m = 40$. The input refractivity profiles are extracted from the (background) refractivity field we used in the previous section; we mimic a grid of stations (0.5° times 0.5° , extending from 7° to 16° in longitude and 47° to 56° in latitude) and extract station-by-station the corresponding input refractivity profile (in total 361 input refractivity profiles). The background refractivity profiles are generated as follows; the background refractivity at zero height corresponds to the input refractivity at zero height adding Gaussian noise with zero mean and a standard deviation of 2% and the background inverse-scale height is taken to be the average of the input inverse-scale heights. The error variance of the background refractivity at zero height equals 2%. The error variance of the background inverse-scale height is approximated by the variance of the input inverse-scale heights. The error covariances of the background are neglected.

Figure 9 shows the fractional refractivity error of the analysis as a function of the height for the observation error 0.03%. The different colors correspond to the different sets of STDs (elevation cut-off angles 0°, 1°, 3°, 7°, 15°, and 90°). For comparison the fractional refractivity error of the background as a function of the height is shown as well. Clearly, there is a benefit of the STDs on top of the ZTD. The information gain strongly depends on the elevation cut-off angle; the lower the elevation cut-off angle, the better the refractivity retrieval. In particular, STDs near the horizon (elevation angles $\leq 3^\circ$) allow a significantly better refractivity retrieval than the ZTD. Yet, we did not pay attention to the observation error. Figure 10 shows the fractional refractivity error of the analysis as a function of the height for the observation error 0.3%. Still, there is a benefit of the STDs on top of the ZTD but the information gain is strongly reduced. Obviously, the observation error overshadows the vertical gradient information that is hidden in the STDs. In principle, we arrive at the same conclusion as Lowry *et al.* [2002]; vertical profiling of refractivity using a single station requires accurate STDs near the horizon (elevation angles $\leq 3^\circ$) because they contain most of the vertical gradient information. The experiment by Lowry *et al.* [2002] and our simulation (so far) left out an important fact; the refractivity field is, in general, not spherically layered (see Figure 6).

A few iterations (typically less than 10) are sufficient. We perform the following simulation cycle; compute a set of true STDs given the true (input) refractivity profile, add noise to mimic observed STDs, and utilize the observed STDs and the background refractivity profile to obtain the analysis (output) refractivity profile. The simulation cycle is repeated for different input refractivity profiles. The root-mean-square deviation between the output and the input refractivity as a function of the height measures to what extent we can extract profile information from the STDs. We experiment with different sets of STDs; i.e., we compute STDs with an elevation angle step size of 1° starting from 90° down to 0° , 1° , 3° , 7° , 15° , and 90° , respectively. In the latter case a single ZTD enters the simulation cycle. This allows us to study the benefit of the STDs on top of the ZTD.

We are free to choose the vertical resolution (Θ) and the number of layers (m) of the refractivity profile. In particular, if the refractivity at zero height is known and a single layer is considered, it is not difficult to see that a single error-free ZTD is

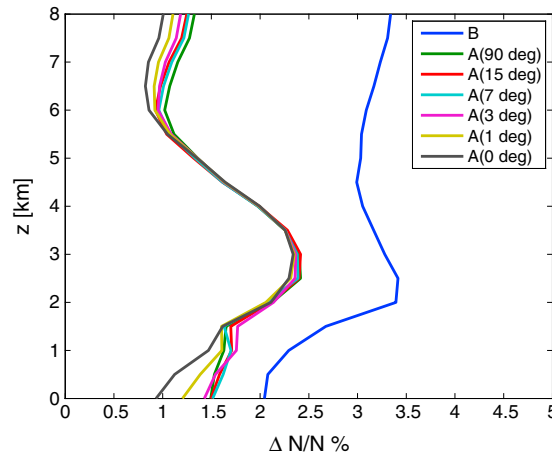


Figure 10. Same as in Figure 9, except that the observation error is 0.3% instead of 0.03%.

operator is expressed in terms of the delay gradient vector, the refractivity at zero height, and the set of inverse-scale heights. The observed STDs stem from the refractivity field; station-by-station we compute a set of STDs (the spacing in azimuth is 30°, and the elevation angles are 3°, 5°, 7°, 10°, 15°, 20°, 30°, 50°, 70°, and 90°) and add Gaussian noise with zero mean and a standard deviation of 0.3%. The background (and first-guess) tropospheric delay gradients are chosen to be 0 mm, and the error variances of the background tropospheric delay gradients are chosen to be 0.5 mm.

Figure 11 shows the fractional refractivity error of the analysis as a function of the height. The different colors correspond to the STDs and the ZTD, respectively. For comparison the fractional refractivity error of the background as a function of the height is shown as well. As expected there is hardly any benefit of the STDs on top of the ZTD (the elevation cut-off angle is 3°, and the observation error is 0.3%). The benefit of STDs on top of the ZTD becomes obvious when we take a look at the retrieved tropospheric delay gradient maps. Figure 12 shows the retrieved tropospheric delay gradient map (red arrows) and the true tropospheric delay gradient map (black arrows). While the retrieved tropospheric delay gradients from the observed ZTDs remain very close to the background tropospheric delay gradients, i.e., no tropospheric delay gradients (not shown), the retrieved tropospheric delay gradients from the observed STDs agree fairly well with the true tropospheric delay gradients. Therefore, unlike extracting vertical gradient information from STDs, extracting asymmetric information from STDs appears to be a less ambitious goal.

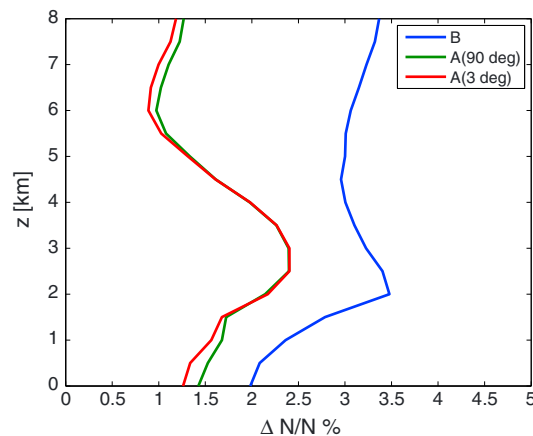


Figure 11. Same as in Figure 9, except that the observation error is 0.3% instead of 0.03% and tropospheric delay gradients are retrieved from the STDs as well.

Next, we drop the simplifying assumption of a spherically layered refractivity field. The observed STDs which enter the simulation cycle do not stem from a single refractivity profile but stem from the refractivity field (they are calculated utilizing the full forward operator), and we consider the following task: given observed STDs estimate the refractivity profile and the tropospheric delay gradients. Therefore, the state vector \mathbf{x} includes the delay gradient vector, the refractivity at zero height, and the set of inverse-scale heights, i.e., $\mathbf{x} = [G_e, G_n, N_0, \xi_1, \dots, \xi_m]$. The corresponding forward operator reads as

$$H[\mathbf{x}] = S_R(N_0, \xi_1, \dots, \xi_m) + \Gamma(G_e, G_n) \quad (27)$$

where Γ accounts for the asymmetry of STDs (refer to Appendix B). The tangent linear (adjoint)

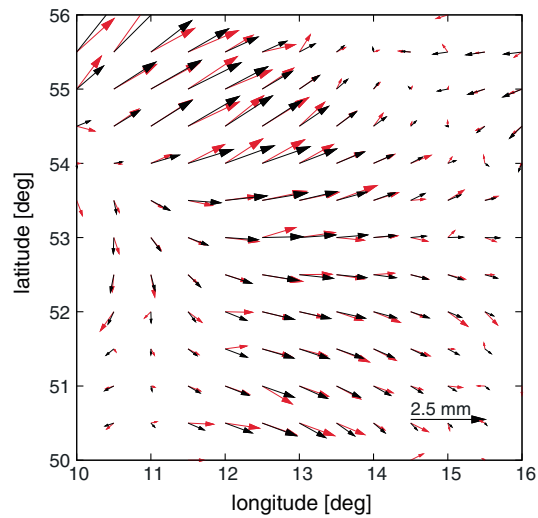


Figure 12. Map of tropospheric delay gradient vectors in the vicinity of Potsdam (26 June 2013, 12 UTC). The red (black) arrows correspond to the retrieved (true) tropospheric delay gradient map. At each location a station provides a set of STDs with an observation error of 0.3%. For details, refer to the text.

4. Comparison of GPS and NWM STDs

The developed algorithm represents a rapid and accurate forward operator and as such it allows the efficient one-to-one comparison of GPS and NWM STDs. For example, Figure 13 shows the fractional deviation between GPS and NWM STDs (top) and the fractional number of data points (bottom) as a function of the elevation angle. The data are collected from 200 stations in Germany, correspond to ± 10 min around 0, 6, 12, and 18 UTC and cover a time period from 25 to 30 June 2014. More than 500,000 STDs enter the statistics. The GPS STDs are estimated from zero-differenced phase observations utilizing GFZs latest Earth Parameter and Orbit Determination System software [Gendt *et al.*, 1999]. The NWM STDs are computed from the IFS analysis of the ECMWF utilizing the forward operator. In good agreement with Zus *et al.* [2012] we find that the fractional deviation between GPS and NWM STDs is about constant. From the standard deviation we estimate an upper bound for the observation error; for the considered geographical region and season this is about 0.5%. The observation error and observation geometry in our simulations are motivated by such comparisons.

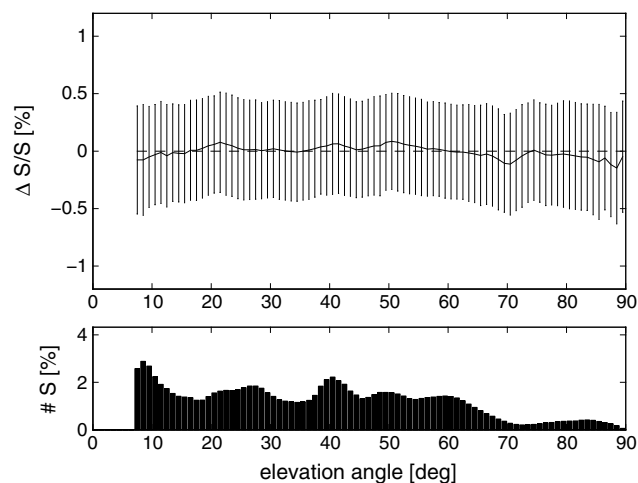


Figure 13. (top) The fractional deviation between GPS and NWM STDs as a function of the elevation angle. The black line indicates the mean deviation, and the error bars indicate the ± 1 sigma deviation from the mean deviation. (bottom) The fractional number of STDs as a function of the elevation angle. The data are collected from about 200 stations in Germany, correspond to ± 10 min around 0, 6, 12, and 18 UTC and cover a time period from 25 to 30 June 2014. More than 500,000 STDs enter the statistics. The elevation cut-off angle of the GPS STDs is 7° .

5. Conclusion

At first let us put the data throughput of the developed forward operator into perspective; given 1000 stations and 30 station-satellite links per station (GPS, GLONASS, and Galileo) than all STDs are computed in 10 s (assuming that the elevation angles are $\geq 3^\circ$). This data throughput is obtained on an ordinary PC using a single core. The accuracy of the algorithm is estimated to be on the 1 mm level close to the zenith and on the 1 cm level for an elevation angle of 5° .

Having developed a fast and accurate forward operator we construct the tangent linear operator and its adjoint for inverse modeling. We test the functionality of the operators in a simulation. This simulation also reveals the benefit of a set of STDs over the ZTD for a single station. Since the developed operators are both rapid and accurate they are tailored for three (four)-dimensional variational data assimilation. Clearly, the developed operators can be used for GNSS travel time tomography [see, e.g., *Bender et al.*, 2010] as well. It must be kept in mind, however, that the reconstruction of the atmospheric state from STDs is an ill-posed problem. In particular, the densification of station networks and the combination of data from the GNSS constellation will allow a more robust estimation of the atmospheric state from STDs [see, e.g., *Bender et al.*, 2011].

In this work we performed simulation studies. We cannot run advanced assimilation studies because we do not have a data assimilation system. Weather agencies do have such systems. We will provide the source codes upon request.

Appendix A: Estimating the Minimum of the Cost Function

Let \mathbf{x}_i denote the refractivity field at the iteration step i . Linearizing the cost function C in the vicinity of the refractivity field \mathbf{x}_i leads to

$$C[\mathbf{x}] = \frac{1}{2} (\mathbf{x} - \mathbf{x}_b)^T \mathbf{B}^{-1} (\mathbf{x} - \mathbf{x}_b) + \frac{1}{2} (\mathbf{y} - H[\mathbf{x}_i] - \mathbf{H}[\mathbf{x}_i](\mathbf{x} - \mathbf{x}_i))^T \mathbf{R}^{-1} (\mathbf{y} - H[\mathbf{x}_i] - \mathbf{H}[\mathbf{x}_i](\mathbf{x} - \mathbf{x}_i)) \quad (\text{A1})$$

The gradient of the cost function C with respect to the refractivity field \mathbf{x} reads as

$$\frac{\partial C}{\partial \mathbf{x}} = \mathbf{B}^{-1} (\mathbf{x} - \mathbf{x}_b) - \mathbf{H}^T[\mathbf{x}_i] \mathbf{R}^{-1} (\mathbf{y} - H[\mathbf{x}_i] - \mathbf{H}[\mathbf{x}_i](\mathbf{x} - \mathbf{x}_i)) \quad (\text{A2})$$

Therefore, the refractivity field \mathbf{x}_{i+1} at the iteration step $i + 1$ is obtained by solving the system of linear equations

$$\mathbf{P}[\mathbf{x}_i] (\mathbf{x}_{i+1} - \mathbf{x}_i) = \mathbf{H}^T[\mathbf{x}_i] \mathbf{R}^{-1} (\mathbf{y} - H[\mathbf{x}_i]) - \mathbf{B}^{-1} (\mathbf{x}_i - \mathbf{x}_b) \quad (\text{A3})$$

where

$$\mathbf{P}[\mathbf{x}_i] = \mathbf{B}^{-1} + \mathbf{H}^T[\mathbf{x}_i] \mathbf{R}^{-1} \mathbf{H}[\mathbf{x}_i] \quad (\text{A4})$$

If we consider a single iteration, choose the first guess refractivity field to be equal to the background refractivity field, that is $\mathbf{x}_0 = \mathbf{x}_b$, and make use of a variant of the Sherman-Morrison-Woodbury formula

$$\mathbf{P}[\mathbf{x}_b]^{-1} \mathbf{H}^T[\mathbf{x}_b] \mathbf{R}^{-1} = \mathbf{B} \mathbf{H}^T[\mathbf{x}_b] (\mathbf{H}[\mathbf{x}_b] \mathbf{B} \mathbf{H}^T[\mathbf{x}_b] + \mathbf{R})^{-1} \quad (\text{A5})$$

the most probable refractivity field is obtained through

$$\mathbf{x}_a = \mathbf{x}_b + \mathbf{B} \mathbf{H}^T[\mathbf{x}_b] (\mathbf{H}[\mathbf{x}_b] \mathbf{B} \mathbf{H}^T[\mathbf{x}_b] + \mathbf{R})^{-1} (\mathbf{y} - H[\mathbf{x}_b]) \quad (\text{A6})$$

Appendix B: Estimating Tropospheric Delay Gradients

The asymmetry of STDs, denoted Γ , is approximated by [*Chen and Herring*, 1997]

$$\Gamma = m(\epsilon) [G_e \sin(\alpha) + G_n \cos(\alpha)] \quad (\text{B1})$$

where G_n and G_e denote the so-called north-south and east-west delay gradient, respectively, m denotes the gradient mapping function, and ε and α denote the elevation and azimuth angle, respectively.

Given a set of STDs, denoted S , and a set of STDs determined under the assumption of a spherically layered refractivity field, denoted S_R , the delay gradient vector $G = (G_e, G_n)$ is obtained by a least squares adjustment

$$G = (\mathbf{f}_j^T \mathbf{W} \mathbf{f}_j)^{-1} \mathbf{f}_j^T \mathbf{W} (S - S_R) \quad (\text{B2})$$

where \mathbf{f}_j denotes the Jacobian. The weight matrix \mathbf{W} is chosen to be

$$W_{ij} = \sin(\varepsilon_i) \sin(\varepsilon_j) \delta_{ij} \quad (\text{B3})$$

such that the representative errors of Γ at low elevation angles are taken into account. The set of STDs consists of STDs with elevation angles 3°, 5°, 7°, 10°, 15°, 20°, 30°, 50°, 70°, and 90°, and the spacing in azimuth is 30°. The map of tropospheric delay gradients is obtained by repeating this procedure for the underlying grid points. As an aside, it should be mentioned that the equation above can be viewed as a forward operator for GPS tropospheric delay gradients.

Acknowledgments

The GFS analysis data are provided by the National Centers for Environmental Prediction (<http://nomads.nccdc.noaa.gov/data/gfsanl>). The IFS analysis data are provided by the European Centre for Medium-Range Weather Forecast (<http://www.ecmwf.int/en/forecasts/datasets/dataset-i-i-atmospheric-fields-high-resolution-forecast>). This work is a contribution to the COST ES1206 project. Reviewers are gratefully acknowledged for their comments.

References

- Bender, M., G. Dick, M. Ge, Z. Deng, J. Wickert, H. G. Kahle, A. Raabe, and G. Tetzlaff (2010), Development of a GNSS water vapour tomography system using algebraic reconstruction techniques, *Adv. Space Res.*, *47*, 1704–1720, doi:10.1016/j.asr.2010.05.034.
- Bender, M., R. Stosius, F. Zus, G. Dick, J. Wickert, and A. Raabe (2011), GNSS water vapour tomography—Expected improvements by combining GPS, GLONASS and Galileo observations, *Adv. Space Res.*, *47*(5), 886–897.
- Bennitt, G. V., and A. Jupp (2012), Operational assimilation of GPS zenith total delay observations into the Met Office Numerical Weather Prediction models, *Mon. Weather Rev.*, *140*, 2706–2719, doi:10.1175/MWR-D-11-00156.1.
- Bevis, M., S. Businger, T. A. Herring, C. Rocken, R. A. Anthes, and R. Ware (1992), GPS meteorology: Remote sensing of atmospheric water vapor using the Global Positioning System, *J. Geophys. Res.*, *97*, 15,787–15,801.
- Chen, G., and T. A. Herring (1997), Effects of atmospheric azimuth asymmetry on the analysis of space geodetic data, *J. Geophys. Res.*, *102*(B9), 20,489–20,502, doi:10.1029/97JB01739.
- Daley, R. (1991), *Atmospheric Data Analysis*, Cambridge Atmos. and Space Sci. Ser., Cambridge Univ. Press, Cambridge, U. K.
- Deng, Z., M. Bender, F. Zus, M. Ge, G. Dick, M. Ramatschi, J. Wickert, U. Löhnert, and S. Schön (2011), Validation of tropospheric slant path delays derived from single and dual frequency GPS receivers, *Radio Sci.*, *46*, RS6007, doi:10.1029/2011RS004687.
- Eresmaa, R., S. Healy, H. Järvinen, and K. Salonen (2008), Implementation of a ray-tracing operator for ground-based GPS Slant Delay observation modeling, *J. Geophys. Res.*, *113*, D11114, doi:10.1029/2007JD009256.
- Gendt, G., G. Dick, and W. Söhne (1999), GFZ analysis center of IGS—Annual report 1998, in *IGS 1998 Technical Reports*, edited by K. Gowey, R. Neilan, and A. Moore, pp. 79–87, Jet Propul. Lab., Pasadena, Calif.
- Giering, R., and T. Kaminski (1998), Recipes for adjoint code construction, *ACM Trans. Math. Software*, *24*, 437–474.
- Hofmann-Wellenhof, B., H. Lichtenegger, and J. Collins (1992), *GPS: Theory and Practice*, Springer, New York.
- Järvinen, H., R. Eresmaa, H. Vedel, K. Salonen, S. Niemel, and J. de Vries (2007), A variational data assimilation system for ground-based GPS slant delays, *Q. J. R. Meteorol. Soc.*, *133*, 969–980, doi:10.1002/qj.79.
- Lowry, A. R., C. Rocken, S. V. Sokolovskiy, and K. D. Anderson (2002), Vertical profiling of atmospheric refractivity from ground-based GPS, *Radio Sci.*, *37*(3), 1041, doi:10.1029/2000RS002565.
- Nafisi, V., et al. (2012), Comparison of ray-tracing packages for troposphere delays, *IEEE Trans. Geosci. Remote Sens.*, *50*(2), 469–481.
- Polli, P., P. Moll, F. Rabier, G. Desroziers, B. Chapnik, L. Berre, S. B. Healy, E. Andersson, and F. -Z. El Guelai (2007), Forecast impact studies of zenith total delay data from European near real-time GPS stations in Meteo France 4DVAR, *J. Geophys. Res.*, *112*, D06114, doi:10.1029/2006JD007430.
- Thayer, G. D. (1974), An improved equation for the radio refractive index of air, *Radio Sci.*, *9*, 803–807.
- Vedel, H., and X-Y Huang (2004), Impact of ground based GPS data on numerical weather prediction, *J. Meteorol. Soc. Jpn.*, *82*(1B), 459–472.
- Wu, X., X. Wang, and D. Lü (2014), Retrieval of vertical distribution of tropospheric refractivity through ground-based GPS observation, *Adv. Atmos. Sci.*, *31*(1), 37–47, doi:10.1007/s00376-013-2215-z.
- Zus, F., G. Beyerle, S. Heise, T. Schmidt, J. Wickert, and C. Marquardt (2011), Validation of refractivity profiles derived from GRAS raw-sampling data, *Atmos. Meas. Tech.*, *4*, 1541–1550, doi:10.5194/amt-4-1541-2011.
- Zus, F., M. Bender, Z. Deng, G. Dick, S. Heise, M. Shang-Guan, and J. Wickert (2012), A methodology to compute GPS slant total delays in a numerical weather model, *Radio Sci.*, *47*, RS2018, doi:10.1029/2011RS004853.
- Zus, F., G. Dick, J. Dousa, S. Heise, and J. Wickert (2014a), The rapid and precise computation of GPS slant total delays and mapping factors utilizing a numerical weather model, *Radio Sci.*, *49*, 207–216, doi:10.1002/2013RS005280.
- Zus, F., G. Dick, J. Dousa, and J. Wickert (2014b), Systematic errors of mapping functions which are based on the VMF1 concept, *GPS Solut.*, *19*, 277–286, doi:10.1007/s10291-014-0386-4.